Device

Article

Physical computing across magnetic and RF domains for passive wireless information retrieval

Graphical abstract

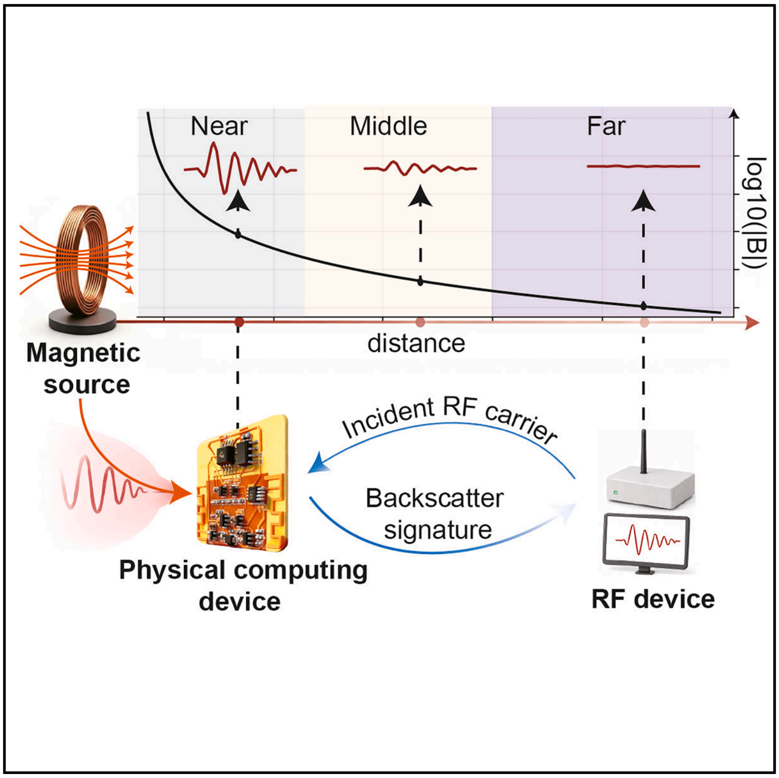

Authors

Long Tan (谭龙), Xiuzhen Guo (郭秀珍), Junying Huang (黄俊颖), Binghe Li (李冰河), Chaojie Gu (顾超杰), Yuanchao Shu (舒元超), Jiming Chen (陈积明)

Correspondence

guoxz@zju.edu.cn (X.G.),
ycshu@zju.edu.cn (Y.S.),
cjm@zju.edu.cn (J.C.)

In brief

Tan et al. present a device that converts magnetic signals into wireless radio signatures by keeping the signal path fully analog. Using a $34 \times 25 \times 10$ mm^3 flexible prototype, a hundred-meter-scale transmission of near-field magnetic acoustic signals at 208.5 μW is developed while reducing system complexity through analog-domain signal processing. The signal path itself performs sensing, compression, and transmission, and the device retrieves magnetic information over long distances at microwatt power.

Highlights

- Passive device converts local magnetic signals into RF backscatter
- Physical computing avoids on-device digital signal processing
- Magnetic information is retrieved over a hundred meters at microwatt-level power
- Receiver-side neural reconstruction recovers intelligible speech

Explore
Early prototypes with exciting performance and new methodology

Tan et al., 2026, Device *4*, 101241
September 18, 2026
https://doi.org/10.1016/j.device.2026.101241

CellPress

Please cite this article in press as: Tan et al., Physical computing across magnetic and RF domains for passive wireless information retrieval, Device (2026), https://doi.org/10.1016/j.device.2026.101241

Device

CellPress

Article

Physical computing across magnetic and RF domains for passive wireless information retrieval

Long Tan (谭龙),[1] Xiuzhen Guo (郭秀珍),[1,3,*] Junying Huang (黄俊颖),[1] Binghe Li (李冰河),[1] Chaojie Gu (顾超杰),[1] Yuanchao Shu (舒元超),[1,*] and Jiming Chen (陈积明)[1,2,*]

[1]College of Control Science and Engineering, Zhejiang University, Hangzhou, Zhejiang 310027, China

[2]College of Automation, Hangzhou Dianzi University, Hangzhou, Zhejiang 310018, China

[3]Lead contact

*Correspondence: guoxz@zju.edu.cn (X.G.), ycshu@zju.edu.cn (Y.S.), cjm@zju.edu.cn (J.C.)

https://doi.org/10.1016/j.device.2026.101241

THE BIGGER PICTURE Low-frequency, near-field magnetic signals can pass through water, biological tissue, and walls, making them attractive for sensing and communication where light and sound have limited performance. Yet magnetic signals decay with distance. Extending their reach requires active wireless sensor nodes that convert weak signals into digital data, process them with microcontrollers, and transmit them via radios. This works, but repeated conversions across analog, digital, and radio-frequency domains increase power consumption and hardware complexity while limiting system lifetime and continuous deployment.

Here, we use analog devices to build physical operators that directly map analog signals to radio-frequency scattering signatures, replacing some of the operations assigned to digital electronics. Local magnetic information is stabilized via analog fusion, exported as radio-frequency backscatter without on-device analog-to-digital conversion, digital processing, or active RF generation.

SUMMARY

Wireless magnetic sensors extend their range through mixed-signal pipelines that rely on repeated conversions between the analog and digital domains, digital processing, and active radio-frequency (RF) transmission, which raise power and system complexity. Here, we report a passive physical computing architecture that directly transforms near-field magnetic signals into RF scattering signatures without digital processing. The system combines adaptive magnetic fusion, comparison-driven analog encoding, and oscillator-free backscatter modulation to reshape and project magnetic waveforms into the RF domain through intrinsic circuit dynamics. A lightweight neural model at the receiver reconstructs the original signal from its physically computed representation. We demonstrate hundred-meter-scale transmission of magnetic acoustic signals at microwatt-level power. This cross-domain physical computing approach provides a scalable foundation for passive magnetic interfaces and distributed magnetic sensor networks.

INTRODUCTION

Low-frequency magnetic fields offer advantages for communication and sensing, including improved penetration through water, biological tissue, and other conductive, lossy media that strongly attenuate high-frequency electromagnetic waves through conductive loss, dielectric loss, and the skin effect, as well as immunity to optical and acoustic interference. These properties have motivated their use in applications such as underwater links,[1–5] human-machine interfaces,[6–10] contactless authentication,[11–13] and biomedical monitoring.[14–16] However, the near-field coupling mechanisms that allow magnetic signals to be highly localized also lead to rapid spatial attenuation,[17,18] limiting their propagation distance. As a result, long-range or distributed magnetic systems remain challenging, particularly in settings where energy consumption, device size, or continuous operation impose stringent constraints.

Existing platforms for magnetic signal acquisition and transmission rely almost exclusively on mixed-signal embedded architectures.[2,19,20] In these designs, analog magnetic waveforms must be digitized by analog-to-digital converters (ADCs), buffered in microcontroller memory, processed and repackaged through digital algorithms, and reconverted to the analog domain using digital-to-analog converters (DACs) for wireless transmission. This repeated domain conversion creates an architectural overhead, establishing an energy floor that constrains system lifetime and limits scaling to large-area or continuously deployed networks. The digital processing pipeline forces magnetic

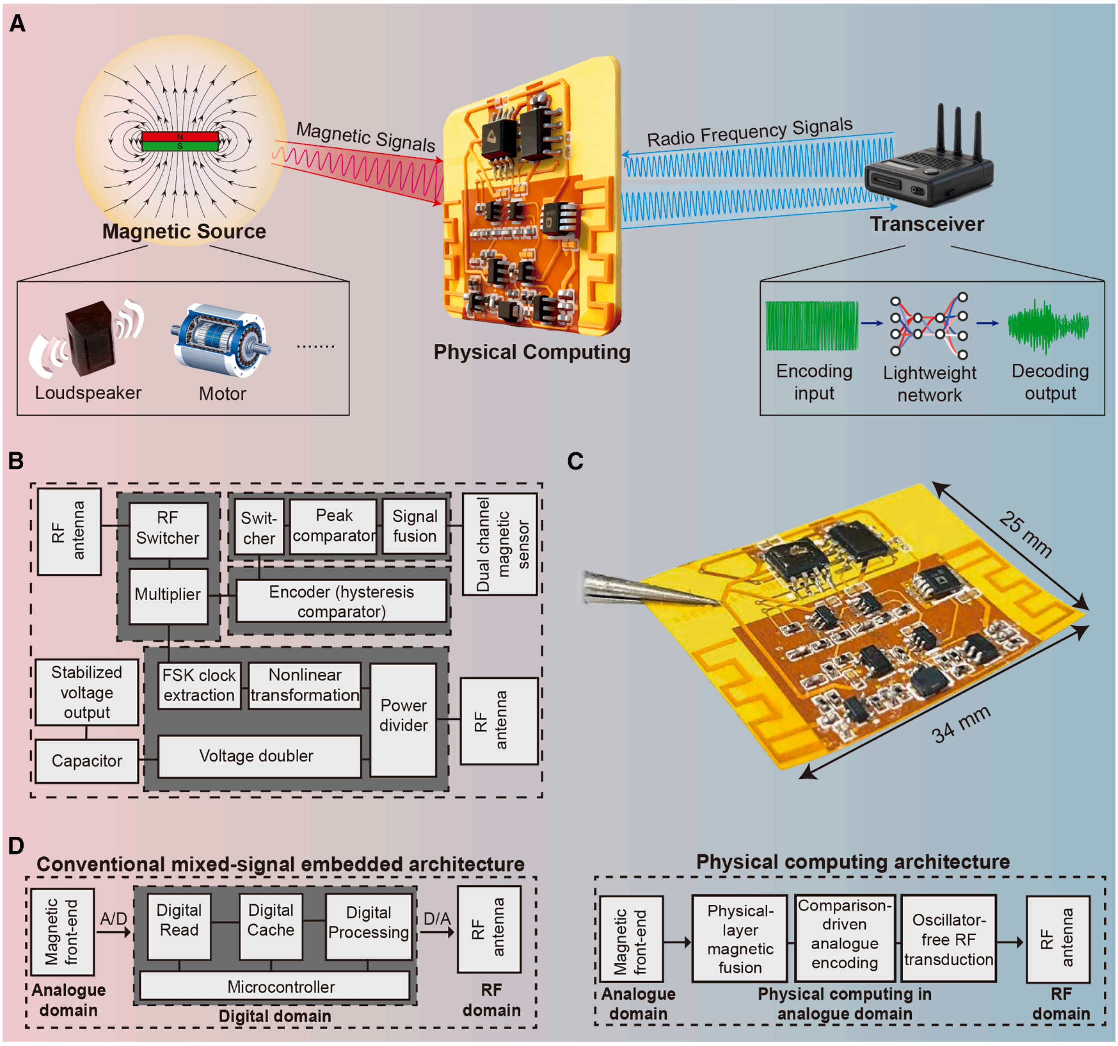

Figure 1. Architecture of cross-domain physical computing

(A) Overall schematic of the passive physical computing that unifies magnetic signal fusing, analog comparison-driven transformation, and oscillator-free radio-frequency (RF) backscatter to establish a direct link between the magnetic and RF domains. A lightweight neural reconstruction model at the receiver recovers the original magnetic waveform from its transmitted physical representation.

(B) Block diagram showing the main hardware modules: magnetic signal fusing, hysteresis-comparator encoder, RF clock extraction, frequency-shift keying (FSK) backscatter modulation, and RF energy harvesting.

(C) Photograph of the fully integrated prototype on a flexible printed circuit board measuring $34 \times 25 \times 10$ mm^3, used in all subsequent experiments.

(D) Comparison of the proposed physical computing architecture with mixed-signal embedded architectures.

systems to function as sensor nodes rather than exploiting the computational structure available in the physical signal path. Magnetoelastic resonant sensors provide another wireless readout architecture in which external magnetic excitation couples to a passive magnetoelastic element and the measured quantity is encoded as a change in resonant response.[21] Because their transduction mechanism relies on tracking resonant-state changes, these sensors are well suited to passive parameter readout but are not designed to preserve and relay the full temporal structure of fast, complex magnetic waveforms.

In this article, we introduce a passive end-to-end device that enables direct cross-domain transformation between near-field magnetic signals and radio-frequency (RF) scattering signatures, allowing long-range, low-power retrieval of local magnetic information over a passive wireless link (Figure 1A). Instead of following mixed-signal embedded architectures, our system embeds computational operators directly into the physical signal path, allowing magnetic information to be continuously processed, reshaped, and projected into the RF domain through intrinsic circuit-level dynamics. We refer to this circuit-level design as a physical computing architecture—one in which computational operations are carried out directly by the analog dynamics of the physical signal path, with no on-device analog-to-digital conversion or digital processing. The architecture consists of a sequence of analog physical operators that realize a structured computational pathway (Figure 1B). An adaptive analog fusion module first performs domain-native computation, such as differential combination, field enhancement, and selective attenuation, to extract salient magnetic components while suppressing irrelevant modes. This is followed by a compact analog transformation stage that maps the fused magnetic waveforms into a high-dimensional spectral representation using comparison-driven, ultra-low-power physical computing primitives. The resulting frequency-domain patterns are then physically transduced into the wireless channel through oscillator-free backscatter modulation, embedding the computed representation into the RF scattering profile with microwatt-level power budgets. At the receiver, a lightweight neural reconstruction model recovers the original magnetic waveform from its transmitted physical representation (see Note S1 for an operator-level formulation of this physical computing pathway).

We fabricate our device on a flexible printed circuit board with a volume of $34 \times 25 \times 10$ mm^3 (Figure 1C) and demonstrate that this passive physical computing architecture can support hundred-meter-scale transmission of magnetic acoustic signals while consuming only microwatt-level power and requiring only a lightweight neural reconstruction model at the receiver (see Video S1 for the outdoor demonstration, Video S2 for the cross-lingual recovery examples, and Video S3 for the non-line-of-sight [NLOS] through-wall experiment). These results indicate that cross-domain physical computing can serve as a scalable foundation for magnetic sensing systems, enabling applications such as magnetic communication, passive sensing interfaces, and large-scale distributed magnetic sensor networks.

RESULTS AND DISCUSSION

Overall system design of the cross-domain physical computing pathway

We validate the proposed physical computing architecture through an integrated prototype that unifies magnetic sensing fusion, comparison-driven analog transformation, and oscillator-free RF transduction within a single continuous passive signal path on a flexible printed circuit board with dimensions of $34 \times 25 \times 10$ mm^3 (see fabrication in the methods). Unlike mixed-signal sensor nodes, the system operates as a unified physical pathway in which magnetic inputs propagate through a cascade of analog operators and are directly projected into the RF scattering domain under continuous external excitation. At the mechanistic level, each analog operator performs a specific mathematical operation directly on the magnetic waveform: the fusion stage forms a vector combination of the two sensing channels and selects the dominant one by conditional decision, the transformation stage applies a threshold comparison that maps the continuous waveform onto a 1-bit sequence while retaining its spectral structure, and the transduction stage exploits diode nonlinearity to mix the signal to a stable RF offset for backscatter. All experimental evaluations are performed at 2.4 GHz under continuous RF excitation with an average incident power of 15 dBm. The total measured power consumption of the complete device is 208.5 μW (see Table S1 and Note S2). The device operates using harvested ambient RF energy, allowing continuous, passive real-time computation. The following subsections characterize each operator in this pathway—magnetic fusion, comparison-driven encoding, and oscillator-free transduction—and conclude with an end-to-end reconstruction benchmark that quantifies information preservation across the physical domain transformation.

Physical-layer magnetic signal fusion

A practical barrier to near-field magnetic sensing is that the measured waveform depends on device orientation relative to the source, which introduces amplitude distortion and degrades any subsequent encoding and wireless transduction (see Note S3). To stabilize magnetic acquisition without digital calibration, we implement a domain-native fusion front end that combines two orthogonally aligned tunnel-magnetoresistance (TMR) channels using analog addition, differential processing, and peak-based selection (Figure 2A). This operation performs computation directly in the magnetic domain by forming the sum and difference of the two sensing channels, then applying a conditional decision that outputs whichever branch is larger, thereby selectively enhancing salient components while suppressing orientation-dependent cancellation (see physical-layer magnetic signal fusion design in the methods).

We characterize the fused response using a loudspeaker coil driven by calibrated sinusoidal and speech-band excitation signals. Loudspeakers provide a readily available and programmable source of audio-correlated magnetic fields (Figure 2B) because the currents driving their voice coils produce time-varying magnetic flux that faithfully follows the input waveform (see Note S3). They produce a three-dimensional magnetic field with a measurable projection onto the two-dimensional sensing plane (Figures 2C and 2D), thereby enabling evaluation of performance across diverse spatial orientations.

Figure 2E illustrates the measured signal strength across varying device orientations. The dual-channel fusion produces a response variation of up to 3.3 dB over a full 360° rotation, outperforming the single-module response that fluctuates by up to 15.4 dB. The fused front end attains 18.9 mV/μT sensitivity through subsequent small-signal amplification, with a power consumption of just 93.8 μW. To evaluate the frequency response of our method, we play a sweep tone ranging from 10 Hz to 4 kHz through the loudspeaker, covering the typical human speech spectrum (300 Hz–3.4 kHz).[22] Figures 2F and 2G compare the frequency responses of the two channels. The output exhibits linear frequency characteristics consistent with the excitation signal, demonstrating that our device tracks magnetic signal variations within the speech frequency range.

We assess the response to speech signals by playing a set of pre-recorded samples and recording the corresponding module outputs. As shown in Figures 2H and 2I, the recorded magnetic signals preserve key spectral features of the original speech waveform. The waveform cosine similarity reaches 98.1%, while the spectral cosine similarity reaches 98.7%, indicating that our device provides a high-fidelity representation of speech dynamics.

Overall, our approach reduces orientation-induced amplitude fluctuations from over 15 dB to about 3 dB while supporting real-time tracking of rapidly varying and complex speech magnetic fields. By stabilizing the input statistics presented to the

Please cite this article in press as: Tan et al., Physical computing across magnetic and RF domains for passive wireless information retrieval, Device (2026), https://doi.org/10.1016/j.device.2026.101241

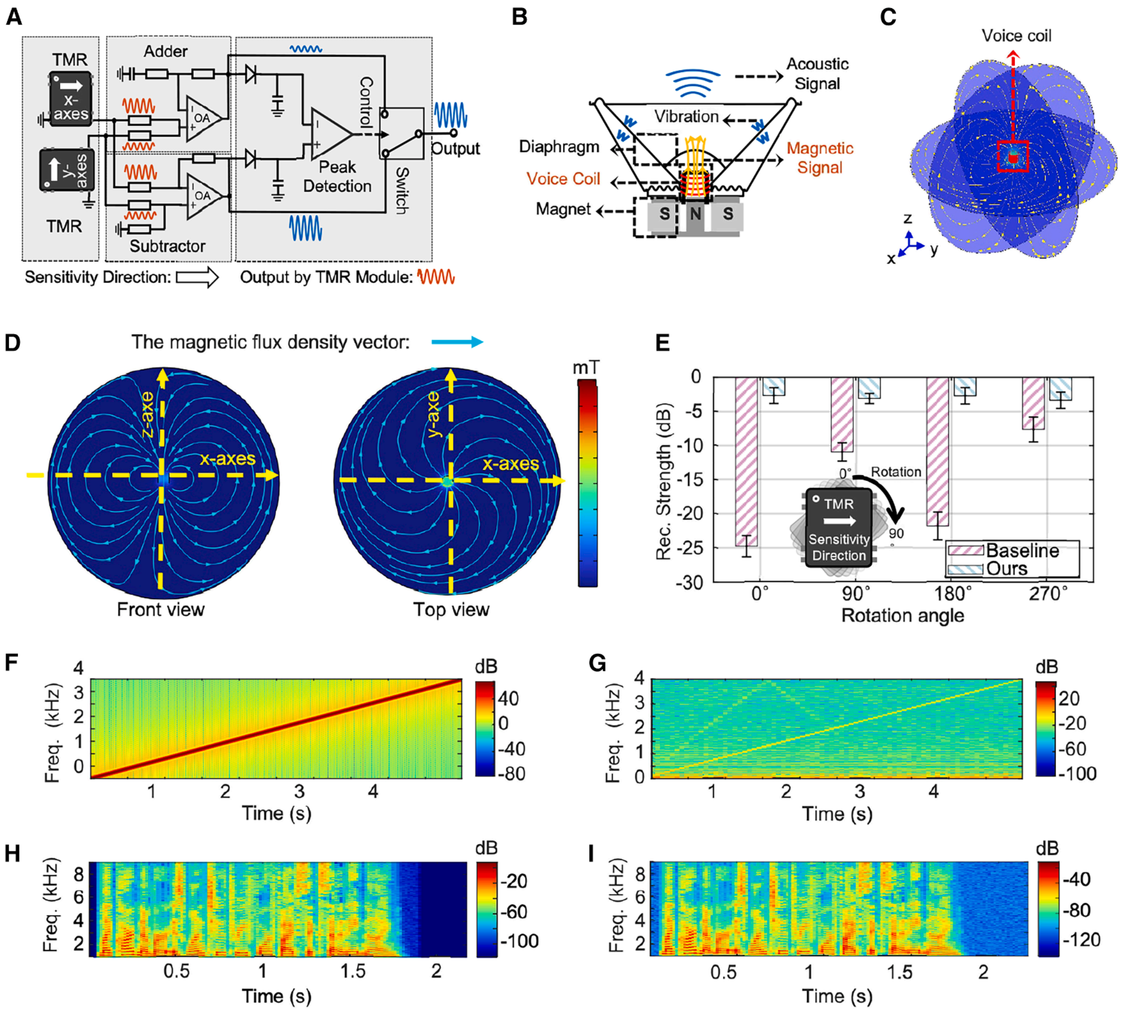

Figure 2. Domain-native magnetic fusion for orientation-robust sensing

(A) Schematic of the adaptive fusion circuit combining two orthogonally aligned TMR channels through analog addition, differential processing, and peak detection to stabilize weak magnetic inputs.

(B) Principle of the programmable loudspeaker used as a magnetic source.

(C) Simulated three-dimensional and planar magnetic-field distributions generated by the coil, confirming measurable in-plane components.

(D) Two-dimensional projection of the magnetic field on the surface plane, shown from the front and top views.

(E) Measured signal amplitude versus sensor orientation. The dual-channel fusion provides uniform response (>-3 dB) compared with a single TMR module, which varies by up to 15.4 dB. The error bars refer to standard deviation.

(F and G) Frequency-response measurement from 10 Hz to 4 kHz using a sweep-tone input, showing linear tracking of magnetic variations within the speech band.

(H and I) Recorded waveforms and spectra under speech excitation. The fused magnetic output preserves key temporal and spectral features of the source (spectral similarity: 98.7%).

downstream computing, the method improves performance stability without introducing the energy or latency overhead associated with digital calibration (see Note S4 for the practical saturation boundary of this operation).

Comparison-driven analog transformation

To transmit magnetic waveforms over long ranges under microwatt budgets, our device must reduce data volume and processing cost before wireless transduction. Rather than digitizing the analog waveform with a multi-bit ADC, we embed a minimal physical computing primitive—temporal comparison—into the signal path (see analog transformation design in the methods). As shown in Figure 3A, the encoder comprises a low-pass filter that extracts a slowly varying reference and a comparator that outputs the sign of the input relative to this reference, generating a 1-bit symbolic sequence:

$$V_{out}(t) = \text{sign}\,(V_{in} - \theta(t))\,, \qquad \text{(Equation 1)}$$

where V_{in} denotes the incoming analog signal and $\theta(t)$ is the comparator threshold. This transformation offers substantial advantages in resilience to interference, preservation of the spectral structure of the original signal, and ultra-low-power operation.

Please cite this article in press as: Tan et al., Physical computing across magnetic and RF domains for passive wireless information retrieval, Device (2026), https://doi.org/10.1016/j.device.2026.101241

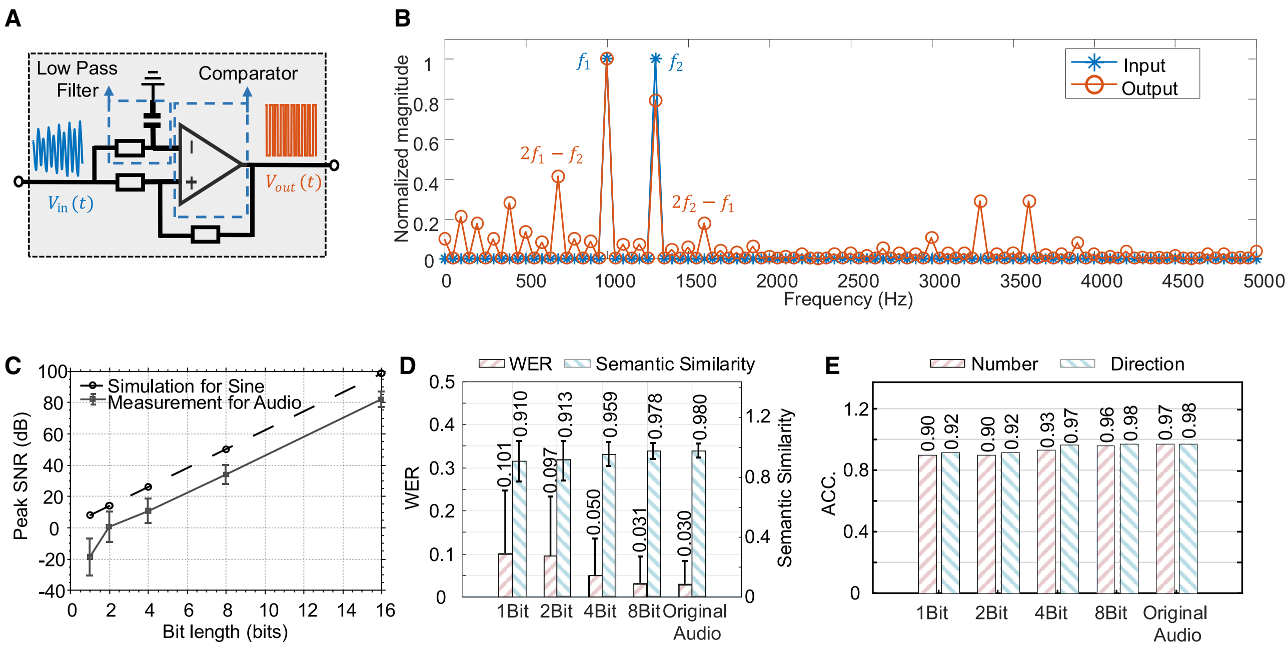

Figure 3. Comparison-driven analog encoding for low-power magnetic signal transformation

(A) Circuit schematic of the encoder consisting of a low-pass filter extracting the signal envelope and a comparator performing differential quantization to generate a 1-bit symbolic output.

(B) Fourier transform of a two-tone input signal (blue, f_1 and f_2) and the encoded output (orange). Input and output signals are sampled at a fixed sampling rate of 16kS/s. The encoded output preserves the main frequency components of the original signal.

(C) Quantization signal-to-noise ratio (SNR) as a function of bit width for simulated and measured data, following the ≈ 6 dB per-bit trend. The error bars refer to standard deviation.

(D) Speech-recognition accuracy and semantic-similarity scores versus encoding bit width, evaluated on the LibriSpeech 100-h dataset. Even 1-bit encoding retains more than 90% semantic similarity while reducing encoding power by over 1000 $\times$ relative to an 8-bit ADC. The error bars refer to standard deviation.

(E) Recognition accuracy of critical semantic elements (numbers and directional terms) as a function of encoding bit width, showing strong preservation of directive semantics even at 1-bit resolution.

We first assess whether this extreme quantization retains useful structure. Specifically, a dual-tone input signal containing two frequency components, f_1 and f_2, is sampled at 16 kS/s. The encoder preserves the primary frequency components of the input signal (Figure 3B), indicating that it captures the spectral structure of the original signal. This frequency retention facilitates monitoring of magnetic field variations, such as motor speed sensing and frequency-modulation-based magnetic communication. For complex magnetic acoustic signals, the structure of speech allows 1-bit encoding to retain sufficient information to support subsequent speech reconstruction.

We have evaluated the performance in terms of both audio encoding noise and semantic preservation. We evaluate the impact of quantization resolution on magnetic signal encoding. As shown in Figure 3C, increasing the quantization bit width enhances the signal-to-noise ratio (SNR), consistent with uniform quantization theory (see Note S5). For instance, 8-bit quantization achieves more than a 52 dB SNR improvement over 1-bit encoding. In contrast, 1-bit encoding implemented using a simple comparator consumes only 1.56 μW—significantly lower than the 1.89 mW required by an 8-bit ADC—enabling energy-efficient, on-device signal encoding.

To evaluate whether such extreme compression still maintains meaningful information, we use the LibriSpeech 100-h corpus as a benchmark. Automatic speech recognition performed on encoded magnetic signals shows that the word-error rate (WER) increases moderately from 0.03 to 0.10 when the bit width decreases from 8 to 1, while semantic similarity (MPNet embeddings) remains >0.9, as shown in Figure 3D. Thus, even with 1-bit encoding, semantic similarity remains >0.9, confirming that the structured nature of magnetic audio signals permits drastic compression without losing essential temporal features. We analyze the impact of our encoder on critical semantic elements in speech, such as numbers and directional terms. We evaluate the recognition accuracy on samples that contain these key components. As shown in Figure 3E, and as the encoding bit width increases, the proportion of samples in which all numbers and directional terms are correctly identified increases from 0.90 to 0.97 and from 0.92 to 0.98, respectively. The experiments demonstrate the strong robustness of our encoder in preserving essential directive semantics. The comparison encoder reduces on-device energy consumption by orders of magnitude while preserving temporally structured cues that remain recoverable after wireless transmission, enabling the subsequent RF

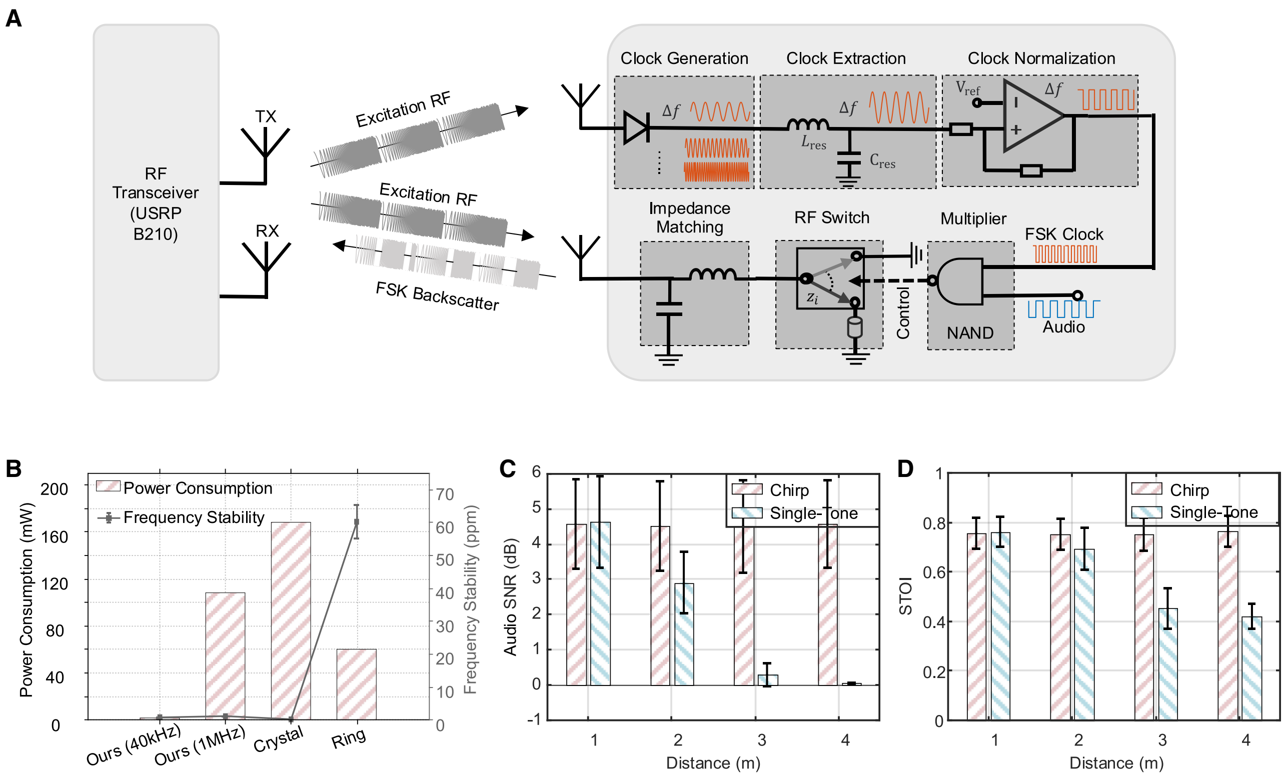

Figure 4. Oscillator-free frequency-shifted backscatter enabled by dual-chirp excitation

(A) Schematic of the backscatter communication module. A dual-chirp excitation signal is transmitted to the device, which harvests a stable frequency-offset clock from the nonlinear mixing output. The device modulates the encoded audio onto the carrier via load impedance switching and reflects the backscatter signal to the receiver for demodulation.

(B) Measured frequency stability and power consumption of different clock mechanisms. Dual-chirp extraction achieves less than 0.2% frequency deviation at 108 μW (1 MHz), matching crystal-reference stability at lower power. The error bars refer to standard deviation.

(C and D) Signal-to-noise ratio (SNR) and short-time objective intelligibility (STOI) as functions of transmission distance under single-tone and dual-chirp excitations. The dual-chirp mode maintains higher fidelity beyond 3 m with microwatt-level consumption. The error bars refer to standard deviation.

transduction stage to operate with microwatt-level budgets (see Note S4 for the operating boundary under low-SNR conditions).

Oscillator-free RF transduction

To propagate the physically encoded signal wirelessly through ultra-low-power backscatter communication, the system must overcome the spectral overlap between incident and backscattered waves.[23,24] Backscatter addresses this by introducing a local oscillator, but oscillators and synthesizers impose additional power and complexity. Instead, we generate the required frequency offset passively by exploiting diode nonlinearities (Figure 4A; see oscillator-free FSK backscatter design in the methods). When two incident RF tones at f_1 and f_2 illuminate the device, nonlinear mixing produces intermodulation components at

$$f_{osc} = |f_1 - f_2|, \quad \text{(Equation 2)}$$

which we harness as an intrinsic modulation clock for frequency-shifting backscatter.

To enhance frequency-offset stability and maintain a constant frequency offset f_{osc}, we introduce a dual-chirp excitation where the instantaneous frequencies sweep synchronously while preserving the offset (see Note S6). This enables stable clock extraction with <0.2% deviation at microwatt power levels (1.56 μW at 40 kHz and 108 μW at 1 MHz), achieving crystal-like stability with lower power (Figure 4B).

The combination of the encoder and the passively generated frequency offset enables the frequency-shift keying FSK backscatter link. The encoded sequence modulates the antenna's load impedance, with reflectivity as

$$\rho_i = \frac{Z_i - Z_a^*}{Z_i + Z_a}, \quad \text{(Equation 3)}$$

where Z_i denotes the i-th impedance state presented to the antenna, Z_a represents the antenna's input impedance, and $(\cdot)^*$ denotes the complex conjugate operation. With the frequency-shifting clock, the backscattered signal is naturally separated from the excitation in the spectral domain, eliminating spectral overlap without synthesizers or digital processing. Representative prior uses of diode nonlinearity include tunnel-diode-based low-power backscatter designs and nonlinearity-enabled cross-frequency communication.[25–27] In contrast, our nonlinear stage is used to derive a stable excitation-referenced offset clock for oscillator-free frequency-shifted backscatter of comparison-encoded magnetic information rather than to sustain bias-dependent oscillation or to realize large-span cross-band translation (see Note S7 for a detailed comparison).

To evaluate the performance of the dual-chirp carrier design, we compare it with a single-tone excitation source as the baseline. We measure the effective range under different excitation carriers in an indoor line-of-sight (LOS) scenario. As shown in Figures 4C and 4D, when the distance reaches 3 m, the baseline method suffers a performance drop, with the SNR decreasing to 0.3 dB and the short-time objective intelligibility (STOI) falling to 0.45. In contrast, within the same range, our method maintains a much higher SNR and STOI, demonstrating enhanced stability and effectiveness. Here, STOI is used to reflect intelligibility-related short-time temporal-spectral preservation. Accordingly, the distance gain observed here should be interpreted as a practical improvement in detectable RF-link performance and magnetic information retrieval rather than as a universal increase in intrinsic backscatter efficiency. This improvement arises mainly from two design choices: the dual-chirp carrier improves interference rejection and yields a frequency-shifted component that is easier to separate from the excitation than a single-tone baseline,[28,29] while 1-bit encoding supports high-contrast binary load modulation and relaxes the detection requirement relative to multi-level amplitude transmission.[30,31]

Overall, the dual-chirp excitation combined with nonlinear mixing provides a robust, oscillator-free frequency-shifted backscatter mechanism that supports microwatt-level wireless transmission of magnetic signals and overcomes the spectral overlap challenge.

End-to-end cross-domain reconstruction in outdoor environments

To evaluate the end-to-end fidelity of the entire physical computing architecture, we employ speech reconstruction from magnetic inputs as a representative benchmark task. Speech signals are selected because they contain rich temporal dependencies and fine spectral details, thereby imposing stringent requirements on time-domain accuracy and frequency preservation. Moreover, speech signals are used in human-machine interfaces, making them a relevant target for low-power magnetic sensing applications.

Figure 5A illustrates the experimental setup for end-to-end evaluation. The programmable magnetic source generates magnetic speech signals, which are captured by our device, encoded, and transmitted via backscatter to a receiver located 103 m away. At the receiver, the demodulated and downsampled encoding sequences are processed by a lightweight denoising neural network (Figure 5B) that reconstructs the analog waveform directly in the time domain (see Figure S1 and Note S8 for the receiver-side processing details and Table S2 and Note S9 for the receiver-side network structure and runtime statistics).

Large-scale experiments over the 100-h dataset confirm consistent enhancement: the averaged SNR rises from –25.8 to 3.5 dB and the average STOI from 0.60 to 0.72, as shown in Figure 5C. Figure 5D presents typical reconstructed signals. Raw received waveforms exhibit significant quantization and channel noise (SNR = –21.6 dB, STOI = 0.69). After neural reconstruction, these metrics improve to 7.2 dB and 0.82, respectively. Spectrogram analysis shows that the recovered audio restores fundamental harmonics and formant structures, demonstrating the preservation of semantic information through the cross-domain link (see Tables S3 and S4 for a direct comparison between demodulation-only recovery and neural reconstruction). Cross-lingual speech recovery examples are further shown in Video S2. Our architecture also supports real-time speech transmission and reconstruction in both indoor and outdoor environments (see Figure S2 and Video S3 for the NLOS setup and corresponding results). These results demonstrate that the physical computing pathway preserves information integrity across magnetic, electronic, and RF domains, enabling high-fidelity reconstruction of complex temporal signals.

Conclusions and outlook

We have developed a cross-domain physical computing architecture that unifies magnetic sensing, analog computation, and wireless transduction in a single passive pathway, establishing an integrated physical computing system for low-power, long-range magnetic-to-RF information retrieval. Instead of mixed-signal embedded architectures, our architecture achieves long-range magnetic information retrieval without digital conversion or active oscillation by directly transforming signals between the magnetic and RF domains.

The demonstration of real-time, long-distance signal retrieval and reconstruction establishes the feasibility of energy-autonomous magnetic interfaces. Because the entire computing chain operates with a total power consumption of only 208.5 μW, the architecture can be powered directly by harvested ambient RF energy, providing a path toward maintenance-free operation. In principle, the same physical-computing framework can be extended to other modalities, such as electric, optical, or mechanical domains, where analog operators can perform computing directly on physical quantities before transduction. Looking ahead, three directions are important for expanding this framework. First, future systems should improve scenario adaptability. Different tasks may require different sensing modalities, signal bandwidths, and information types. Therefore, dedicated analog computing architectures should be designed for specific applications so that sensing, encoding, and transmission can occur directly at the passive device without intermediate digital-domain conversion. Second, the computing capability of a single passive device remains limited. A promising next step is to build arrayed physical computing architectures in which multiple analog computing units operate together to implement higher-dimensional transformations, parallel feature extraction, or even physical domain neural-network operations before wireless transduction. Third, although this work demonstrates magnetic-to-RF information mapping, the same design principle could be extended to other cross-domain pathways, such as electric-to-RF, acoustic-to-RF, optical-to-RF, or mechanical-to-RF transformations. These directions would require task-specific transducers, controllable analog operators, and scalable circuit integration, but they could broaden physical computing from our magnetic-interface platform into a general strategy for low-power distributed sensing and communication.

Overall, our work highlights a scalable paradigm of cross-domain physical computing, in which sensing, computation,

Please cite this article in press as: Tan et al., Physical computing across magnetic and RF domains for passive wireless information retrieval, Device (2026), https://doi.org/10.1016/j.device.2026.101241

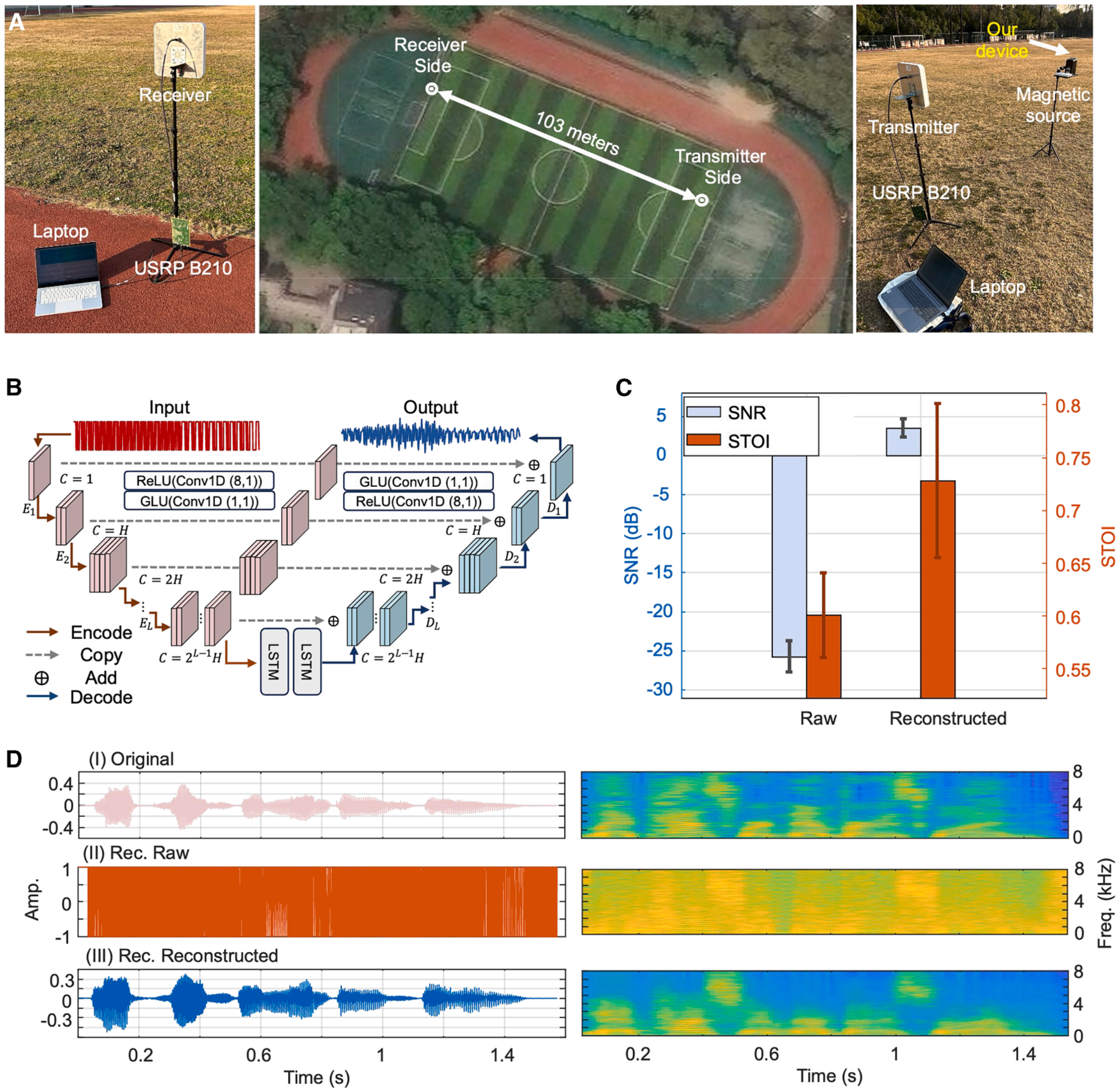

Figure 5. Cross-domain reconstruction benchmark demonstrating end-to-end fidelity

(A) Experimental setup for end-to-end evaluation. Magnetic speech signals generated by a programmable magnetic source are captured by the device, encoded, and transmitted via backscatter to a receiver located 103 m away.

(B) Neural denoising network based on a U-Net backbone that reconstructs time-domain waveforms from demodulated 1-bit sequences.

(C) Overall reconstruction performance on the 100-h LibriSpeech dataset. After neural post-processing, the average SNR improves from –25.8 to 3.5 dB and STOI from 0.60 to 0.72. The error bars refer to standard deviation.

(D) Representative original, raw, and reconstructed waveforms and their spectrograms. The neural model restores harmonic structure and formant patterns, confirming substantial information preservation across magnetic, electronic, and RF domains.

and communication are seamlessly co-designed within the same physical circuit dynamics. Such architectures could form the basis for next-generation distributed sensor networks, adaptive human-machine interfaces, and intelligent ambient systems that operate continuously at ultra-low power.

METHODS

Fabrication of the physical computing architecture

We implement our hardware prototype on a flexible printed circuit board using commercial off-the-shelf (COTS) analog components. The entire hardware integrates the physical computing chain and has a total size of $34 \times 25 \times 10$ mm^3, as shown in Figure 1C. We employ the TMR2901[32] module to capture magnetic signals and utilize the OPA349 operational amplifier[33] to amplify and differentiate captured signals. The LPV7215 comparator[34] is utilized to compare the amplified and differentiated signals and encode the analog signal, enabling efficient encoding for subsequent cross-domain transmission.

The oscillator-free RF transduction module primarily consists of the antenna and RF back end for frequency-shift clock extraction and backscatter communication. We adopt an inverted-F antenna (IFA) with a center frequency of 2.4 GHz as the RF antenna (the circuit implementation and antenna characteristics of the present 2.4 GHz RF system are detailed in Figure S3 and Note S12). The choice of 2.4 GHz as the carrier frequency is motivated by its favorable penetration capability under LOS and through-wall conditions, and the antenna operating at this frequency is physically compact. The carrier frequency is adjustable, and the system can be adapted to other frequency bands by replacing the antenna and tuning the corresponding RF components. The IFA is selected to achieve both a compact form and wide coverage to meet our communication requirements.[35] For the clock extraction circuit, the diode HSMS-282[36] is employed as a nonlinear component, and the low-power comparator TLV3201[37] is used to normalize the extracted signal, with a power consumption of only 108 μW. To achieve backscatter modulation, we utilize the RF switch ADG902[38] to switch the antenna load impedance according to the encoded audio signal and the extracted clock signal, which are combined using a NOT-AND (NAND) gate.[39]

Transceiver side setup

We used USRP B210 software-defined radios (SDRs) to transmit excitation carrier signals and receive the backscattered signals. The received backscattered signals are processed using GNU Radio software (see Notes S8 and S13). The transmission power is set to a default value of 15 dBm. The default excitation signal is configured as a dual-chirp waveform with a center frequency of 2.4 GHz, a spreading factor (SF) of 12, a bandwidth of 250 kHz, and a frequency offset f_{osc} of 1 MHz (the chirp parameters are set according to the LoRa standard protocol). A Lenovo Xiaoxin 16 Pro laptop is employed to demodulate the received signals using Python-based signal processing scripts. The denoising network is implemented using the PyTorch framework and executed on an Ubuntu 22.04 workstation equipped with an NVIDIA GeForce RTX 3090 GPU and the CUDA 12.8 toolkit.

Experimental setup

The system setup is illustrated in Figure 5A. The device is affixed near the target magnetic source in the form of a small sticker. The programmable magnetic source sends the magnetic speech signals, which are captured by our device, encoded, and transmitted via backscatter to a receiver located 103 m away. To ensure the diversity of the speech content, we employ the widely used LibriSpeech dataset[40] to evaluate our device, which comprises a large-scale corpus of over 100 h of recordings from 291 individuals. The training and test data originate from different speakers, ensuring a fair evaluation of generalization.

Simulation setup

The spatial distribution of the magnetic field signal is modeled using COMSOL Multiphysics. A circular coil with radius R = 1 cm is placed in the *x-y* plane, and the driven current is 1 mA. The magnetic flux density is computed according to the Biot-Savart law under quasi-static conditions. The resulting three-dimensional field map confirmed that the in-plane components of the magnetic field remain significant and measurable, as shown in Figures 2C and 2D.

Physical-layer magnetic signal fusion design

The proposed adaptive fusion design consists of two key components: dual-channel sensing and adaptive signal fusion, as shown in Figure 2A.

First, two sensing channels are constructed within the two-dimensional plane to capture the magnetic field components along two orthogonal axes. Each TMR module thus measures the projection of the magnetic signal along its respective sensing axis. Specifically, for a projection angle of 30°, the sensing projections of the *x* axis and *y* axis TMR modules are $\frac{\sqrt{3}}{2}k_0|\mathbf{B_L}|$ and $\frac{1}{2}k_0|\mathbf{B_L}|$, respectively. Similarly, when the projection angle is 120°, the corresponding projections are $-\frac{1}{2}k_0|\mathbf{B_L}|$ and $\frac{\sqrt{3}}{2}k_0|\mathbf{B_L}|$. These results indicate that the two sensing signals cannot be directly summed, as their directional nature introduces phase differences that can degrade overall fusion performance.

Next, adaptive signal fusion is proposed using low-power circuitry, thereby avoiding the computational overhead associated with microcontroller-based ADC sampling and processing. Specifically, the two signals are simultaneously fed into both an adder and a differential circuit to achieve signal fusion. For signals with a projection angle of 120°, the differential circuit effectively amplifies the signal. The fused output is then processed by a peak detection circuit to extract its maximum magnitude, and signal selection is performed by comparing the detected peaks.

Analog transformation design

On the device side, we adopt a hysteresis comparator to achieve ultra-low overhead encoding, as shown in Figure 3A. The encoding circuit consists of a low-pass filter and a comparator. The low-pass filter extracts the direct current (DC) component of the analog audio signal, which serves as the comparison threshold for the comparator. The comparator then outputs a 1-bit-encoded signal based on whether the input signal exceeds the threshold. This design allows for efficient encoding while minimizing power consumption.

Oscillator-free FSK backscatter design

The proposed oscillator-free FSK backscatter comprises three main components: clock generation, clock extraction, and clock normalization, as illustrated in Figure 4A.

First, to generate the clock signals, the excitation carrier is fed into a diode, which acts as a nonlinear component. The signal output from the diode contains multiple chirp components along with a constant-frequency component at f_{osc}, whose amplitude is proportional to A^2, where A denotes the amplitude of the received excitation signal (see Note S6).

To extract the clock signal, we employ a band-pass filter to isolate the desired frequency component at f_{osc}. This is achieved using a passive inductor-capacitor (LC) resonant network that selectively amplifies signals near the target resonance frequency. The resonance frequency satisfies the equation: $f_{res} = \frac{1}{2\pi\sqrt{L_{res}C_{res}}}$, where L_{res} and C_{res} are the inductance and capacitance of the resonant circuit, respectively. Clock extraction can be achieved by adjusting the resonant parameters in accordance with the clock frequency. For 1 MHz clock extraction, the inductance and capacitance of the resonant network are set to 100 μH and 25 pF, respectively.

Please cite this article in press as: Tan et al., Physical computing across magnetic and RF domains for passive wireless information retrieval, Device (2026), https://doi.org/10.1016/j.device.2026.101241

Finally, the extracted signal is passed through a comparator to achieve signal normalization, ensuring that the signal's amplitude is within the desired range. This step enables the clock signal to meet the control threshold, allowing for reliable modulation control while maintaining minimal power consumption.

RESOURCE AVAILABILITY

Lead contact

Requests for further information and resources should be directed to and will be fulfilled by the lead contact, Prof. Xiuzhen Guo (guoxz@zju.edu.cn).

Materials availability

This study did not generate new unique materials.

Data and code availability

The authors declare that the data supporting the findings of this study are available within the article and supplemental information. All original code is available at the Zenodo repository: https://doi.org/10.5281/zenodo.20002486. Any additional information required to reanalyze the data reported in this paper is available from the lead contact upon reasonable request.

ACKNOWLEDGMENTS

This work is supported by the National Science Fund of China under grant nos. 62472379, 62394341, 62394344, and 92467301; the Key Research and Development Program of Zhejiang Province under grant no. 2025C01012; and the Zhejiang Provincial Natural Science Foundation of China under grant no. LR26F020001.

AUTHOR CONTRIBUTIONS

Methodology, L.T. and X.G.; hardware implementation, L.T.; software, L.T.; investigation, L.T. and J.H.; formal analysis, L.T., X.G., and B.L.; writing – original draft, L.T. and X.G.; writing – review & editing, X.G., Y.S., and J.C.; conceptualization, X.G. and Y.S.; supervision, X.G., Y.S., and J.C.; project administration, X.G.; experimental platform construction, J.H.; data curation, B.L.; system design, C.G.; system implementation support, C.G. and J.C.; project leadership, J.C.; research design, Y.S.; funding acquisition, J.C. X.G. serves as the lead contact and a corresponding author, and Y.S. and J.C. serve as corresponding authors. All authors discussed the results, revised the manuscript, approved the final version, and agree to be accountable for all aspects of the work.

DECLARATION OF INTERESTS

The authors declare no competing interests.

DECLARATION OF GENERATIVE AI AND AI-ASSISTED TECHNOLOGIES IN THE WRITING PROCESS

During the preparation of this work, the authors used ChatGPT-5 in order to polish the article and check for syntax errors. After using this tool, the authors reviewed and edited the content as needed and take full responsibility for the content of the publication.

SUPPLEMENTAL INFORMATION

Supplemental information can be found online at https://doi.org/10.1016/j.device.2026.101241.

Received: February 23, 2026
Revised: April 15, 2026
Accepted: June 17, 2026

REFERENCES

1. Cheng, Z., Wang, X., Lv, X., Sun, J., Chu, Z., Zhou, J., and Dong, S. (2025). A Wearable, Ultrasonically-Actuated Magnetic-Dipole Rotating Resonator For Mobile Communication In Cross-Medium Environment. Nat. Commun. *16*, 4137. https://doi.org/10.1038/s41467-025-59539-y.
2. Canales-Gómez, G., León-Gónzalez, G., Jorge-Muñoz, N., Arroyo-Núñez, J.H., Antonio-Yañez, E.D., and Núñez-Cruz, R.S. (2022). Communication System Based On Magnetic Coils For Underwater Vehicles. Sensors (Basel) *22*, 8183. https://doi.org/10.3390/s22218183.
3. Chu, S., Luloff, M.S., Yan, J., Petrov, P., Stevens, C.J., and Shamonina, E. (2021). Magnetoinductive Waves In Attenuating Media. Sci. Rep. *11*, 7679. https://doi.org/10.1038/s41598-021-85838-7.
4. Li, Q., Cui, Z., Ma, X., Yue, W., U, I.H., Zhou, K., Qu, J., Chang, J., Huang, Y., Liu, C., et al. (2025). A Flexible, Magnet-Based Miniaturized Mechanical Antenna Enabling Low-Frequency Cross-Medium Communication Between Unmanned Systems. Commun. Eng. *5*, 15. https://doi.org/10.1038/s44172-025-00569-1.
5. Yang, S., Geng, J., Zhou, H., Wang, K., Zhao, X., Lu, J., Zhao, R., Tang, X., Zhang, Y., Su, D., et al. (2023). Long-Range EM Communication Underwater With Ultracompact ELF Magneto-Mechanical Antenna. IEEE Trans. Antennas Propag. *71*, 2082–2097. https://doi.org/10.1109/TAP.2022.3227799.
6. Wang, L., Wang, W., Dai, H., and Liu, S. (2023). MagSound: Magnetic Field Assisted Wireless Earphone Tracking. Proc. ACM Interact. Mob. Wearable Ubiquitous Technol. *7*, 1–32. https://doi.org/10.1145/3580889.
7. Liu, Y., Huang, C., Wang, K., Qin, Z., and Jin, W. (2025). MIPair: Exploiting Magnetic Induction For Laptop-Phone Pairing. IEEE Trans. Mobile Comput. *24*, 6886–6900. https://doi.org/10.1109/TMC.2025.3546758.
8. Abdelnasser, H., Harras, K.A., and Youssef, M. (2020). MagStroke: A Magnetic Based Virtual Keyboard for Off-the-Shelf Smart Devices. In 2020 17th Annual IEEE International Conference on Sensing, Communication, and Networking (SECON) (Como, Italy: IEEE), pp. 1–9. https://doi.org/10.1109/SECON48991.2020.9158416.
9. Liao, Q., Huang, Y., Huang, Y., Zhong, Y., Jin, H., and Wu, K. (2022). MagEar: Eavesdropping via audio recovery using magnetic side channel. In Proceedings of the 20th Annual International Conference on Mobile Systems, Applications and Services. Portland Oregon (ACM), pp. 371–383. https://doi.org/10.1145/3498361.3538921.
10. Efe Tiryaki, M., Esmaeili-dokht, P., Lazovic, J., Pruessmann, K.P., and Sitti, M. (2025). Nuclear Magnetic Resonance For Wireless Magnetic Tracking. Nat. Commun. *16*, 10840. https://doi.org/10.1038/s41467-025-66468-3.
11. Huang, J., Guo, X., Gu, C., Miao, Y., He, S., Shu, Y., and Chen, J. (2025). MagKey: Empowering Wearables With Ballistocardiography-Based Key Generation Through Magnetic Field Vibration Sensing. Proc. ACM Interact. Mob. Wearable Ubiquitous Technol. *9*, 1–28. https://doi.org/10.1145/3712272.
12. Zhang, Y., Han, D., Li, A., Zhang, L., Li, T., and Zhang, Y. (2023). MagAuth: Secure And Usable Two-Factor Authentication With Magnetic Wrist Wearables. IEEE Trans. Mobile Comput. *22*, 311–327. https://doi.org/10.1109/TMC.2021.3072598.
13. Zhang, Y., Yang, M., Ling, Z., Liu, Y., and Wu, W. (2020). FingerAuth: 3D Magnetic Finger Motion Pattern Based Implicit Authentication For Mobile Devices. Future Gener. Comput. Syst. *108*, 1324–1337. https://doi.org/10.1016/j.future.2018.02.006.
14. Xu, J., Duan, C., Wan, X., Che, Z., Zhao, X., Zhou, Y., Song, Y., Yin, J., Tat, T., Li, S., and Chen, J. (2025). A Soft Magnetoelastic Sensor To Decode Levels Of Fatigue. Nat. Electron. *8*, 709–720. https://doi.org/10.1038/s41928-025-01418-x.
15. Guo, X., Tan, L., Gu, C., Shu, Y., He, S., and Chen, J. (2024). MagWear: Vital Sign Monitoring Based On Biomagnetism Sensing. IEEE Trans. Mobile Comput. *23*, 14918–14933. https://doi.org/10.1109/TMC.2024.3452499.

16. Wan, J., Nie, Z., Xu, J., Zhang, Z., Yao, S., Xiang, Z., Lin, X., Lu, Y., Xu, C., Zhao, P., et al. (2024). Millimeter-Scale Magnetic Implants Paired With A Fully Integrated Wearable Device For Wireless Biophysical And Biochemical Sensing. Sci. Adv. *10*, eadm9314. https://doi.org/10.1126/sciadv.adm9314.

17. Agbinya, J.I. (2013). Investigation Of Near Field Inductive Communication System Models, Channels And Experiments. Prog. Electromagn. Res. B *49*, 129–153. https://doi.org/10.2528/PIERB12120512.

18. Agbinya, J.I. (2022). Wireless Power Transfer (River Publishers).

19. Kim, M.J., Chae, S.H., Shim, Y.B., Lee, D.H., Kim, M.J., Moon, Y.K., and Kwon, K.W. (2019). Design And Implementation Of Magnetic Induction Based Wireless Underground Communication System Supporting Distance Measurement. KSII Trans. Internet Inf. Syst. *13*, 4227–4240. https://doi.org/10.3837/tiis.2019.08.023.

20. Zhou, F., Song, S., Deng, Y., Zhang, T., Chen, B., and Xu, N. (2021). Mixed-Signal Data Acquisition System For Optically Detected Magnetic Resonance Of Solid-State Spins. Rev. Sci. Instrum. *92*, 114702. https://doi.org/10.1063/5.0070135.

21. G Saiz, P., Fernández de Luis, R., Lasheras, A., Arriortua, M.I., and Lopes, A.C. (2022). Magnetoelastic resonance sensors: Principles, applications, and perspectives. ACS Sens. *7*, 1248–1268. https://doi.org/10.1021/acssensors.2c00032.

22. Baken, R.J. (1987). Clinical Measurement of Speech and Voice (College-Hill Press).

23. Zhang, P., Bharadia, D., Joshi, K., and Katti, S. (2016). HitchHike: Practical Backscatter Using Commodity WiFi. In Proceedings of the 14th ACM Conference on Embedded Network Sensor Systems CD-ROM (Stanford CA USA: ACM), pp. 259–271. https://doi.org/10.1145/2994551.2994565.

24. Na, X., Guo, X., Yu, Z., Zhang, J., He, Y., and Liu, Y. (2023). Leggiero: Analog WiFi Backscatter with Payload Transparency. In Proceedings of the 21st Annual International Conference on Mobile Systems, Applications and Services (ACM), pp. 436–449, Helsinki Finland. https://doi.org/10.1145/3581791.3596835.

25. Varshney, A., Soleiman, A., and Voigt, T. (2019). TunnelScatter: Low Power Communication for Sensor Tags using Tunnel Diodes. In The 25th Annual International Conference on Mobile Computing and Networking. Los Cabos Mexico (ACM), pp. 1–17. https://doi.org/10.1145/3300061.3345451.

26. Varshney, A., Yan, W., and Dutta, P. (2022). Judo: Addressing the energy asymmetry of wireless embedded systems through tunnel diode based wireless transmitters. In Proceedings of the 20th Annual International Conference on Mobile Systems, Applications and Services (ACM), pp. 273–286, Portland Oregon. https://doi.org/10.1145/3498361.3538923.

27. An, Z., Lin, Q., and Yang, L. (2018). Cross-Frequency Communication: Near-Field Identification of UHF RFIDs with WiFi. In Proceedings of the 24th Annual International Conference on Mobile Computing and Networking (New Delhi India: ACM), pp. 623–638. https://doi.org/10.1145/3241539.3241569.

28. Peng, Y., Shangguan, L., Hu, Y., Qian, Y., Lin, X., Chen, X., Fang, D., and Jamieson, K. (2018). PLoRa: A passive long-range data network from ambient LoRa transmissions. In Proceedings of the 2018 Conference of the ACM Special Interest Group on Data Communication (Budapest Hungary: ACM), pp. 147–160. https://doi.org/10.1145/3230543.3230567.

29. Song, Y., Lu, L., Wang, J., Zhang, C., Zheng, H., Yang, S., Han, J., and Li, J. (2023). μMote: Enabling Passive Chirp De-spreading and μW-level Long-Range Downlink for backscatter Devices. In 20th USENIX Symposium on Networked Systems Design and Implementation (NSDI 23) (USENIX), pp. 1751–1766.

30. Bletsas, A., Dimitriou, A.G., and Sahalos, J.N. (2010). Improving Backscatter Radio Tag Efficiency. IEEE Trans. Microw. Theor. Tech. *58*, 1502–1509. https://doi.org/10.1109/TMTT.2010.2047916.

31. Thomas, S., and Reynolds, M.S. (2010). QAM backscatter for passive UHF RFID tags. In 2010 IEEE International Conference on RFID (IEEE RFID 2010) (Orlando, FL, USA: IEEE), pp. 210–214. https://doi.org/10.1109/RFID.2010.5467238.

32. Multi Dimension (2024). TMR2901 datasheet. https://www.dowaytech.com/en/res/201906/25/c1d0ea287092004d.pdf.

33. Texas Instruments (2025). OPA349 datasheet. https://www.ti.com/product/OPA349.

34. Texas Instruments (2024). LPV7215 datasheet. https://www.ti.com/product/LPV7215.

35. Nakano, H. (2016). Inverted-F antennas. In Low-profile Natural and Metamaterial Antennas: Analysis Methods and Applications (John Wiley & Sons, Ltd), pp. 59–74. https://doi.org/10.1002/9781118859704.ch4.

36. DigiKey (2025). HSMS282 product page. https://www.digikey.com/en/products/detail/broadcom-limited/HSMS-2820-TR1/697940.

37. Texas Instruments (2025). TLV3201 datasheet. https://www.ti.com/document-viewer/tlv3201/datasheet.

38. Analog Devices (2025). ADG902 datasheet. https://www.analog.com/en/products/adg902.html.

39. Texas Instruments (2025). SN74AUP1G00 datasheet. https://www.ti.com.cn/document-viewer/cn/sn74aup1g00/datasheet.

40. Panayotov, V., Chen, G., Povey, D., and Khudanpur, S. (2015). Librispeech: An ASR corpus based on public domain audio books. In 2015 IEEE International Conference on Acoustics, Speech and Signal Processing (ICASSP) (IEEE), pp. 5206–5210. https://doi.org/10.1109/ICASSP.2015.7178964.